Peer reviewed version

University of Bristol - Explore Bristol Research
General rights

Bio-Inspired Distributed Strain and Airflow Sensing For Small Unmanned Air Vehicle Flight Control

Sergio A. Araujo-Estrada,[*] Francis Salama,[*] Colin Greatwood,[*]
Kieran Wood,[*] Thomas Richardson[†] and Shane P. Windsor[‡]

Department of Aerospace Engineering, University of Bristol, UK

Flying animals such as birds, bats and insects all have extensive arrays of sensory organs distributed in their wings which provide them with detailed information about the airflow over their wings and the forces generated by this airflow. Using two small modified unmanned air vehicle platforms (UAVs), one with a distributed array of 12 strain gauge sensors and one with a chord-wise array of 4 pressure sensors, we have examined the distribution of the strain and air pressure signals over the UAV wings in relation to flight conditions, including wind tunnel testing, indoor free flight and outdoor free flight. We have also characterised the signals provided by controlled gusts and natural turbulence. These sensors were then successfully used to control roll motions in the case of the strain sensor platform and pitch motions in the case of the pressure sensor platform. These results suggest that distributed mechanosensing and airflow sensing both offer advantages beyond traditional flight control based on rigid body state estimation using inertial sensing. These advantages include stall detection, gust alleviation and model-free measurement of aerodynamic forces. These advantages are likely to be important in the development of future aircraft with increasing numbers of degrees of freedom both through flexibility and active morphing.

I.   Introduction

Small unmanned air vehicles (UAVs) flying in an urban setting face a difficult aerodynamic environment due to turbulence, with air speed possibly fluctuating rapidly by more than 40% at rooftop altitudes.[1] As small UAVs fly relatively slowly and have wing spans of a similar scale as much of the turbulence, large changes in wind angle can occur over the wing span of the aircraft. For a small fixed wing UAVs with a conventional wing layout, this primarily generates strong disturbances in roll.[2] Most current attitude control systems for small UAVs use signals from an intertial measurement unit (IMU) to measure the rate of angular rotation, as well as linear acceleration, in three axes. This scheme works well for larger aircraft, but often cannot respond fast enough to stabilize small UAVs in turbulence due to the smaller inertia of the aircraft and the relatively greater turbulent aerodynamic forces.[2]

Birds, bats and insects all have extensive sensor arrays in their wings which give them information about the distribution of air flow over their wings and the force distribution this creates within their wings. In terms of flow sensors birds have on the order of hundreds of vibration sensors, known as Herbst corpusles, throughout their wings which provide information about flow conditions over their feathers.[3] Bats have flow sensitive hairs distributed across the membranes of their wings which respond to flow direction and velocity.[4] While insects have arrays of flow sensitive hairs all over their bodies and wings.[5] In terms of force, or strain sensors, birds and bats have muscles spindle fibres which give sensory feedback about the strains in their wing muscles,[6] while insects have campaniform sensilla which are thought to provide similar information.[5] Overall, it is thought that this information helps animals to deal with the windy, gusty conditions that they often experience, allowing them to tailor their wing movements to the moment by moment wind conditions.[7]

---

[*]Research Associate.
[†]Senior Lecturer in Flight Mechanics.
[‡]Lecturer in Aerodynamics/Aeroelasticity.

A number of studies have already shown some of the potential benefits of incorporating measurements of force and flow into the attitude control systems of small fixed wing UAVs. Distributed arrays of pressure sensors have been shown to offer the potential for improved performance in a number of different studies. In some cases the pressure is integrated over the surface to provide measurements of the forces and/or moments acting on the aircraft.[8-10] While in other cases the sensors comprise part of a flush air data system used to give estimates of aerodynamic state variables such as air speed, angle of attack and sideslip.[11,12] There have also been investigations into the potential advantages offered by unconventional flow sensors such as artificial hair based flow velocity sensors.[13,14] The use of force or strain sensing has also been explored, but not to the same extent, with studies showing that a small number of strain sensors could potentially offer advantages for attitude control based on total moment measurement, both theoretically[15] and experimentally.[16]

This paper presents results of ongoing research investigating the potential application of bio-inspired distributed sensing to improve the flying qualities of small scale fixed wing UAVs. The rest of this paper is organised as follows: Section II presents the experimental methods and platforms used for this research and their main characteristics. Section III presents results from wind tunnel tests carried out to characterise the strain and pressure signals. Section IV presents feedback control experimental results using the strain and pressure instrumented platforms. Section V summarises the information presented in this paper, and discusses areas of potential application for distributed sensing.

II.   Experimental Setup

Two separate platforms, one with a distributed strain sensor array and one with a distributed pressure sensor array were developed. These two platforms were based on modified radio controlled aircraft airframes which were then instrumented with distributed sensors, amplifiers and control hardware. The strain sensing aircraft was first used in wind tunnel testing to characterise the response of the strain sensors under different loading conditions, before being used in free flight testing. In free flight testing the strain signal characteristics in response to a controlled gust were analysed, before developing and testing a closed-loop roll control system. The pressure sensing aircraft was used to characterise the pressure signal characteristics in response to angle of attack using wind tunnel testing. This was followed by the implementation and testing of dynamic wind tunnel pitch control testing, using a customised version of an autopilot preprogrammed pitch controller. This controller uses an estimated angle of attack as control input, two approaches were used to obtain the estimated angle of attack: one using inertial-based measurements and another using pressure measurement.

A.   Experimental Platforms

To perform the strain sensing experiments a Hobbyking's® Easy Sky glider radio controlled airplane was used as base platform. While the pressure sensing experiments were performed using a Hobbyking's® Bixler 2 radio controlled airplane.

The Easy Sky glider is a battery powered high wing, push propeller model used as a radio controlled beginner's model. The airplane has three control surfaces: elevator, rudder and ailerons. The control surfaces are controlled by servomotors. Figure 1(a) shows a picture of the Easy Sky glider while installed in the $7' \times 5'$ wind tunnel at the University of Bristol. The Bixler 2 is a battery powered mid wing, push propeller model used as a radio controlled beginner's model. The airplane has four control surfaces controlled by servomotors: elevator, rudder, ailerons ands flaps. Figure 1(b) shows a picture of the Bixler 2 while installed in the Open-Jet wind tunnel at the University of Bristol. The main characteristics of the out-of-the-box Sky Easy glider and Bixler 2 are given in Table 1.

To acquire the strain data and pressure data, along with the aircraft's motion data, a flight data acquisition system was integrated. Figure 2 shows a schematic diagram of the flight data acquisition system. The system consists of of two main parts: a strain/pressure data acquisition system and an autopilot computer.

The strain data acquisition system is composed of four subsystems, namely the sensing, amplification, acquisition and remote logging subsystems. In the case of the strain sensing platform, the sensing subsystem consists of arrays of strain gauges (N2A-06-S061P-350, Micro-Measurements) arranged in a full-bridge configuration along the wing of the aircraft. They measure the strain directly and output an electrical signal proportional to the strain. The amplification subsystem consists of signal conditioning and amplification modules (DCELL DLCHMCAN, Mantracourt). Each module is directly connected to a sensing unit (strain or pressure), sampling the signal at regular intervals. The DCELL modules are connected to a CAN bus that

American Institute of Aeronautics and Astronautics
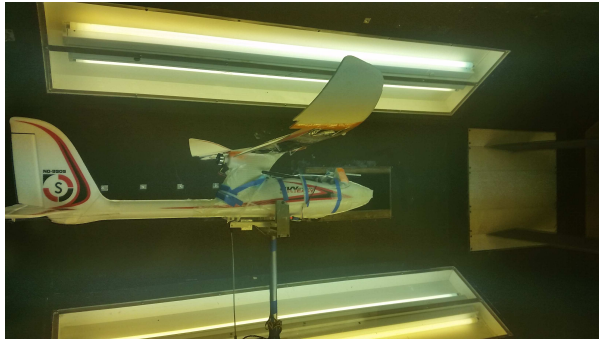
(a) Strain sensing platform in $7' \times 5'$ wind tunnel

(b) Pressure sensing platform in Open-Jet wind tunnel

Figure 1. UAV platforms installed in the University of Bristol wind tunnels.

Table 1. Sky Easy glider and Bixler 2 main characteristics

Parameter	Value	
	Easy Sky	Bixler 2
Weight	$0.370\,\mathrm{kg}$	$0.760\,\mathrm{kg}$
Wing area	$0.152\,\mathrm{m}^2$	$0.260\,\mathrm{m}^2$
Wing span	$1.050\,\mathrm{m}$	$1.500\,\mathrm{m}$
Length	$0.863\,\mathrm{m}$	$0.963\,\mathrm{m}$
Wing load	$2.44\,\mathrm{kg\,m}^{-2}$	$2.923\,\mathrm{kg\,m}^{-2}$

provides data transmission and reception capabilities. The acquisition subsystem consists of a development board (chipKIT Max32, Digilent) based on a PIC32 micro-controller. The micro-controller polls the DCELL modules at regular intervals to acquired the strain data. The strain data is encoded and then transmitted to both the autopilot and the remote logging subsystem. The remote logging subsystem is formed by two XBee WiFi modules (aircraft and base nodes), a WiFi Access Point and a personal computer. The aircraft node receives the strain data from the acquisition subsystem, the aircraft node transmits the data to the base node and finally the the data is logged by the personal computer.

The pressure data acquisition system consists of two subsystems: the sensing and acquisition subsystems. Figure 2 shows a schematic diagram of this simplified data acquisition system, represented by the box in grey dashed line. For the pressure sensing platform, the sensing subsystem consists of an array of 4 pressure sensors positioned chord-wise in the right wing of the aircraft. Their output electrical signal is proportional to the local gauge pressure. The acquisition subsystem in the pressure sensing platform is identical as the one for the strain sensing one except that the sensor signals are acquired through the built-in ADC in the PIC32 micro-controller.

For both platforms, a Pixhawk (3DR) is used as an autopilot computer to perform flight control tasks and to log the strain/pressure data along with the aircraft's motion data.

B. Strain Sensing

A total of twelve strain units (strain gauge full-bridge and DCELL amplifier), were installed along an aluminium spar. The aluminium spar was embedded on the wing of the aircraft at approximately the quarter chord line. Table 2 gives the location of each strain unit along the span of the wing and Figure 3(a) shows the Easy Sky glider instrumented wing and approximate location of each strain unit along the wing. Sensors installed on the right semi-wing have been labeled RX, while those installed on the left semi-wing have been labeled LX, with $X = 0, \ldots, 5$.
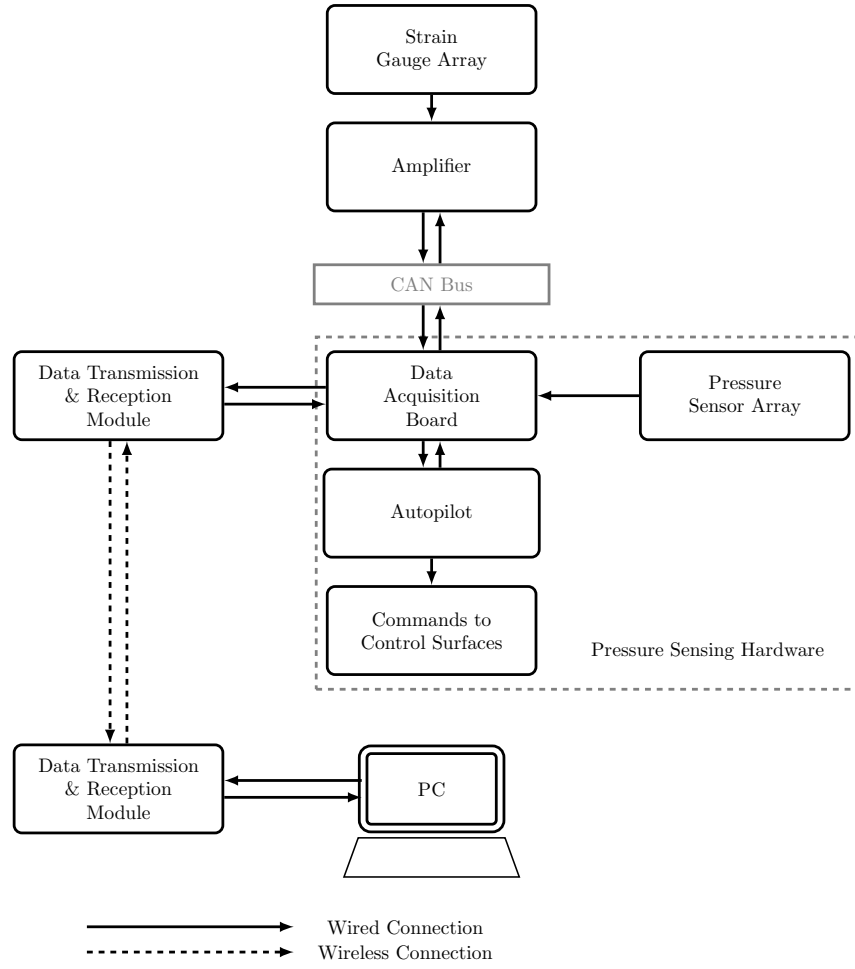
American Institute of Aeronautics and Astronautics

Figure 2. Data acquisition hardware schematic diagram.

Table 2. Location of strain units along wing span

Sensor	Semi-span-wise position from centre [%]	Sensor	Semi-span-wise position from centre [%]
$L0$	-61	$R0$	61
$L1$	-50	$R1$	50
$L2$	-38	$R2$	38
$L3$	-27	$R3$	27
$L4$	-15	$R4$	15
$L5$	-4	$R5$	4

C.   Air Pressure Sensing

A total of four pressure sensors (Freescale Semiconductor MPXV7002 $\pm 2\,\mathrm{kPa}$ pressure sensors), were located inside the fuselage of the aircraft. The pressure sensors were connected via silicon tubing to four corresponding pressure ports within a 3D printed aerofoil wing-insert at the locations given in Table 3. Figure 3(b) shows the Bixler 2 instrumented wing and the approximate location of each pressure sensor on the wing-insert. Sensors $PS01$ and $PS02$ measured the pressure on the upper surface, while sensors $PS03$ and $PS04$ measured the pressure on the lower surface.

American Institute of Aeronautics and Astronautics
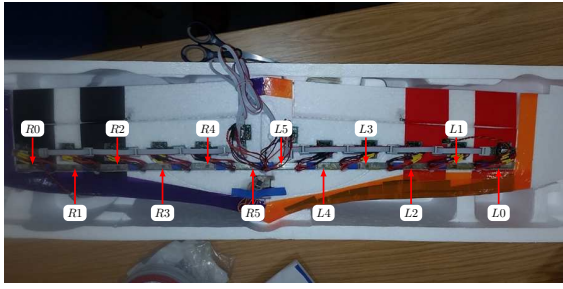
(a) Easy Sky glider instrumented wing.
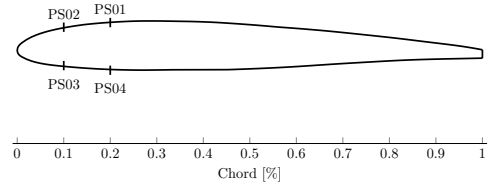
(b) Chordwise location of pressure ports on Bixler 2 instrumented wing.

Figure 3. UAV platforms sensors location.

Table 3. Location of pressure sensors in wing-insert

Sensor	Chord-wise position [%]	Semi-span-wise position from centre [%]
$PS01$	20	10.3
$PS02$	10	10.3
$PS03$	10	10.3
$PS04$	20	10.3

The pressure sensing platform is equipped with an angle of attack vane connected to a potentiometer that provides a voltage reading proportional to the relative angle between the vane and the aircraft body.

III. Signal Characterisation Results

A series of static wind tunnel tests were carried out to obtain the main longitudinal aerodynamic characteristics of both airframes. The tests allowed the characterization of the strain signals and pressure signals change w.r.t the angle of attack of each platform. For these experiments, both airframes were mounted on a force measuring rig. The strain sensing platform was installed in the University of Bristol $7' \times 5'$ closed section wind tunnel, as shown in Figure 1(a). The pressure sensing platform was installed in the University of Bristol open-jet wind tunnel, as shown in Figure 1(b).

The force measuring rig allowed for pitch motion. The motion was driven by a servomotor controlled by the on-board autopilot and/or commanded remotely via a personal computer outside the wind tunnel. The rig included a six component force and moment load cell (AMTI MC3A-500, Advanced Mechanical Technology Inc.). The forces and moments data was acquired, conditioned, amplified and digitized using proprietary hardware and software and stored in the personal computer.

Each test series consisted on a series of steps in angle of attack with the airframe being held at each test point for 10 s for the strain sensing tests and for 20 s for the pressure sensing tests. This ensured that both the load cell and the strain/pressure data are synchronized and removed any dynamic effects from the measurements. Both the strain and pressure data were acquired using the data acquisition system, the strain data was logged remotely using the remote logging subsystem and the pressure data was logged by the autopilot. The strain platform test started with the airframe at an angle of attack of $0°$, while the initial angle of attack of the pressure platform test was $-6°$.
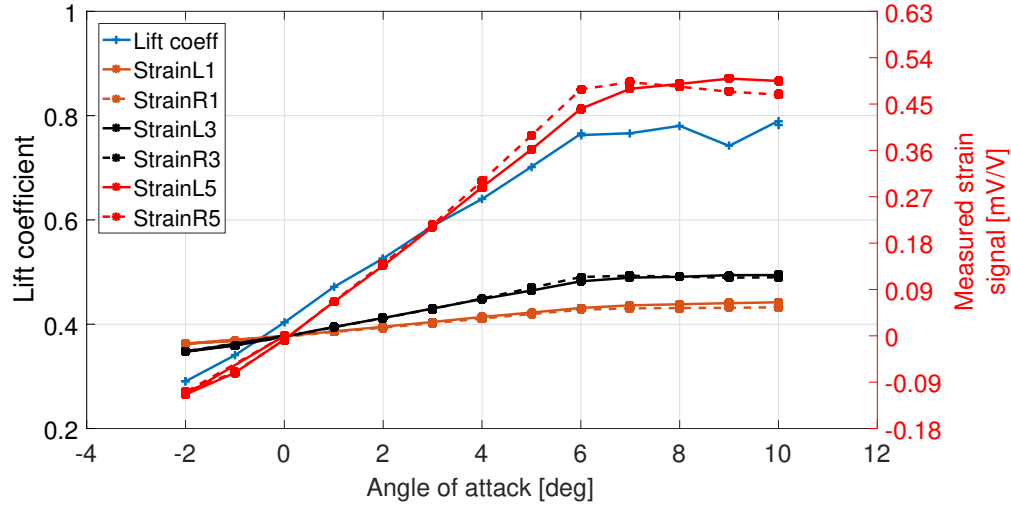
A. Strain Characterisation

Figure 4 shows results obtained from wind tunnel characterisation, using the strain sensing Easy Sky aircraft. The wind speed in this test was $10\,\mathrm{m\,s^{-1}}$. For clarity only six of the twelve measured signals are shown,

American Institute of Aeronautics and Astronautics

namely those from sensors $L1$, $R1$, $L3$, $R3$, $L5$ and $R5$. The strain signals shown in Figure 4, represent the change w.r.t. the measured signal at $0°$ angle of attack.
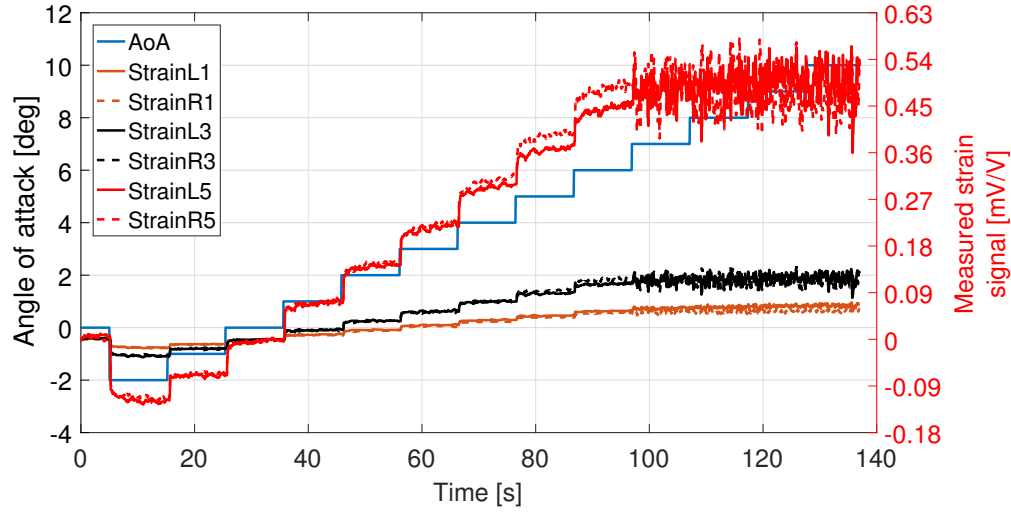
(a) Angle of attack and strain signal time histories

(b) Lift coefficient and strain signal w.r.t angle of attack

Figure 4. Wind tunnel characterisation results for Easy Sky at $10\,\mathrm{m\,s^{-1}}$.

Figure 4(a) shows the angle of attack and strain signal time histories for a wind tunnel characterisation test. In this Figure, the left side scale aids in tracing changes in angle of attack (blue solid line) and the right side scale aids in tracing changes in the strain signals (dashed lines, various colours). The initial angle of attack used for the test was $-2°$, with an increment of $1°$ and a final angle of attack equal to $10°$. It can be observed that, in the region delimited by $5\,\mathrm{s} \leq t \leq 65\,\mathrm{s}$, the strain signal changes proportionally w.r.t the angle of attack. Then, in the region delimited by $65\,\mathrm{s} \leq t \leq 95\,\mathrm{s}$, a significant difference between the signals measured by sensors $L5$ and $R5$ can be observed. In the region delimited by $95\,\mathrm{s} \leq t \leq 135\,\mathrm{s}$, oscillatory behaviour in the measured strain signals can be observed for four of the sensors: $L3$, $R3$, $L5$ and $R5$.

Figure 4(b) shows the lift coefficient and strain signal w.r.t angle of attack obtained in a wind tunnel characterisation test. In this Figure, the left side scale aids in tracing changes in lift coefficient (blue solid line) and the right side scale aids in tracing changes in the strain signals ('*' markers, various colours), with each of the markers representing the average measured strain signal for each angle of attack setting. The lift coefficient exhibits a linear behaviour w.r.t. the angle of attack in the region delimited by $-2°$ and $6°$, with

American Institute of Aeronautics and Astronautics

stall appearing at an angle of attack greater than $6°$. The strain signals also show a linear behaviour w.r.t. the angle of attack in the region delimited by $-2°$ and $6°$. Sensors $L5$ and $R5$ display the biggest change in magnitude as they are the ones closer to the wing root.

An experiment was carried out in the $7' \times 5'$ wind tunnel to explore the detection of a controlled gust using the strain sensing platform. The strain sensing platform was rigidly attached to the force measuring rig previously described in Section II. A set of computer controlled wall-to-wall symmetric aerofoil wings were used to provide the gust, with input frequency and amplitude of $5\,\mathrm{Hz}$ and $20°$, respectively. Figure 5 shows the time histories of the strain platform response to a gust. Figure 5(a) shows the effect on the lift force change due to the gust as measured by the load cell. A Mexican hat wavelet-like shape response can be observed. Figures 5(a) and 5(b) show the effect of the gust on the strain signal measured by the sensors installed on the left and right wing, respectively. All 12 sensors successfully detect the gust, with roots sensors $L5$ and $R5$ showing the biggest change in magnitude. Furthermore, the strain signal wave form matches that measured by the load cell. The strain signal sampling rate ($20\,\mathrm{Hz}$), limits the extend of analysis. However, these results show that strain sensing can be used to detect gusts under controlled conditions.
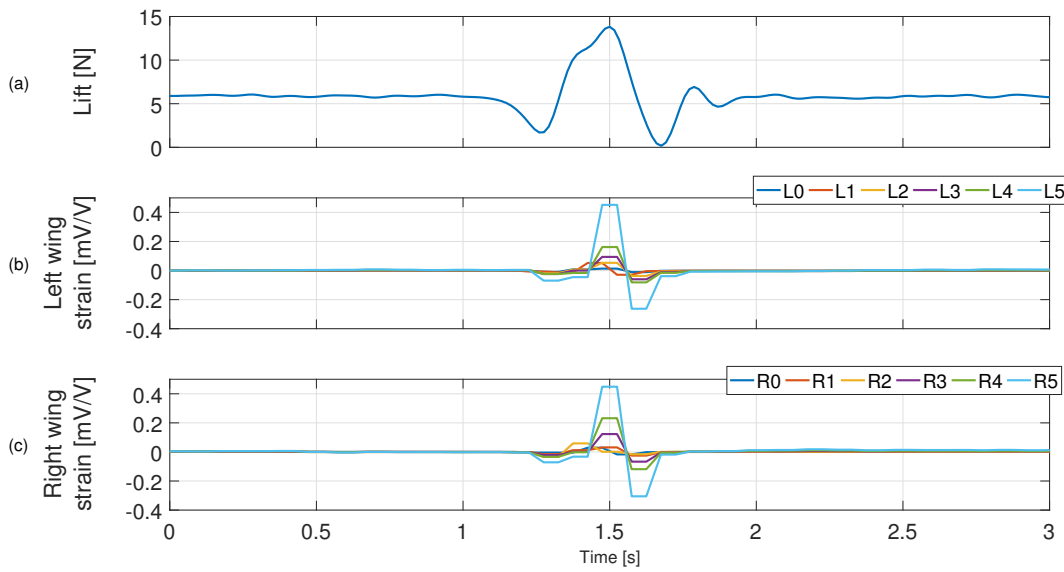

Figure 5. Strain platform response to gust in wind tunnel experiment.

An outdoor flight experiment was carried using the strain sensing platform to characterise the strain signals under "real-life" conditions. For this experiment, data from the strain, inertial and control outputs, was sampled at $50\,\mathrm{Hz}$, while the control inputs data was sampled at $10\,\mathrm{Hz}$. To stabilise the aircraft's motion the autopilot controller was switched on.

Figure 6 shows the time histories response of the strain sensing platform to aileron commands in an outdoor flight experiment. Figure 6(a) shows the response of the aircraft to pilot-commanded aileron doublets. Note the difference in amplitude and waveform between the aileron output and input, this is due to the use of a scaling-down factor to reduce amplitude of motion. The response is dominated by roll motion, as indicated by the amplitude of the body-axes rate measurements. Figure 6(b) shows a detailed view of the aileron output and roll rate time histories. The input-output correlation between aileron and roll rate is easier to observe in this plot and shows the roll rate proportional response to the aileron output, albeit with small time lag. Figure 6(c) shows the time histories of the aileron output and the strain signal difference, namely $L5 - R5$, $L3 - R3$ and $L1 - R1$. Scaling factors of 1, 1.5 and 1.7 have been used for $L5 - R5$, $L3 - R3$ and $L1 - R1$, respectively. The strain signal difference $L3 - R3$ and $L1 - R1$, change proportionally w.r.t. the aileron output, albeit with small time lag. The strain signal difference $L5 - R5$ shows little change, this small change could be explained by the semi-rigid connection between the wing and the fuselage, i.e. wing root moves with body. Figure 6(d) shows the time histories of the roll rate and the strain signal difference.

American Institute of Aeronautics and Astronautics

A difference in phase can be observed between the roll rate and the strain signal difference $L3 - R3$ and $L1 - R1$. These results show that strain sensing can be used to model multi-DOF wing motion/deformation.
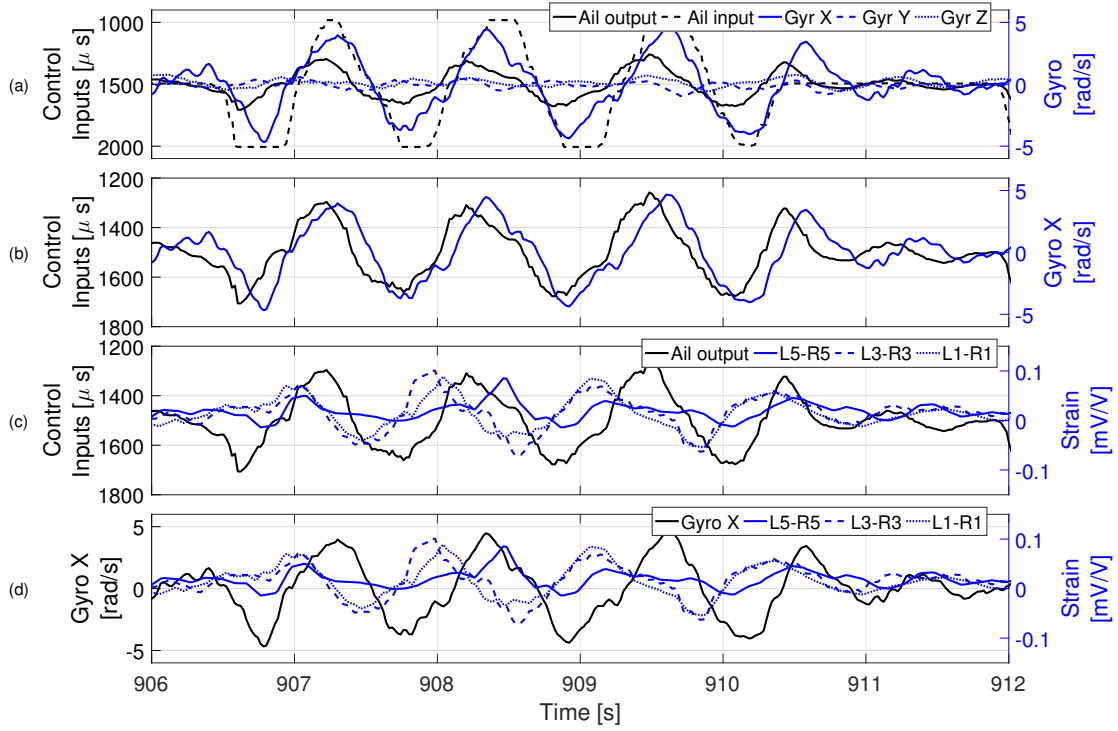

Figure 6. Strain sensing outdoor flight results: response to aileron commands.

Figure 7 shows the time histories response to a natural gust, of the strain sensing platform in an outdoor flight experiment. Figure 7(a) shows the time histories of the aileron output, aileron input and body rates. When compared to Figure 6(a), it can be observed that the input from the pilot is vary small. However, at $t \approx 945\,\text{s}$ a significant change in roll rate is observed, this is easier to observe in Figure 7(b). This change in roll rate is followed by a response from the autopilot to compensate this change. Note that the roll rate leads the aileron output signal and has opposite sign, indicating a response to an external perturbation, i.e. a natural gust. Figure 7(c) shows the time histories of the aileron output and the strain signal difference, the scaling factors remain the same as those previously mentioned. In this case, the signal $L5 - R5$ shows significant change in magnitude coincident with change in input. Note difference in magnitude when compared to Figure 6(c). Figure 7(d) shows the time histories of the roll rate and the strain signal difference. Signal $L5 - R5$ almost coincides with roll rate signal. These results suggest that strain sensing can be used to detect natural gusts.

B. Air Pressure characterisation

Figure 8 shows the results for a wind tunnel characterisation test, using the pressure sensing Bixler aircraft at a wind speed of $16\,\text{m s}^{-1}$. In this test, the initial angle of attack, α was set as $-6°$. Then, it was slowly increased and maintained at predetermined values for 20 s each time, up to $\alpha 14°$. Then, α was slowly decreased and once again maintained at predetermined values for 20 s each time, until it returned to its initial value. Figure 8(a) shows the measured pressure signal time histories for sensors $PS01$, $PS02$, $PS03$, and $PS04$, these represent differential pressure. It can be observed that for $0\,\text{s} \leq t \leq 600\,\text{s}$, the top surface pressure decreases as α increases and that the lower surface pressure increases as α increases. Evidence of flow separation can be observed in Figure 8(a) for $650\,\text{s} \leq t \leq 750\,\text{s}$, as indicated by the pressure drop in the signals from sensors $PS01$ and $PS01$.

Figure 8(b) shows the measured pressure signal as a function of angle of attack, as well as the pressure values computed using XFOIL[17] for a Reynolds number equal to that of the experiment. In the region
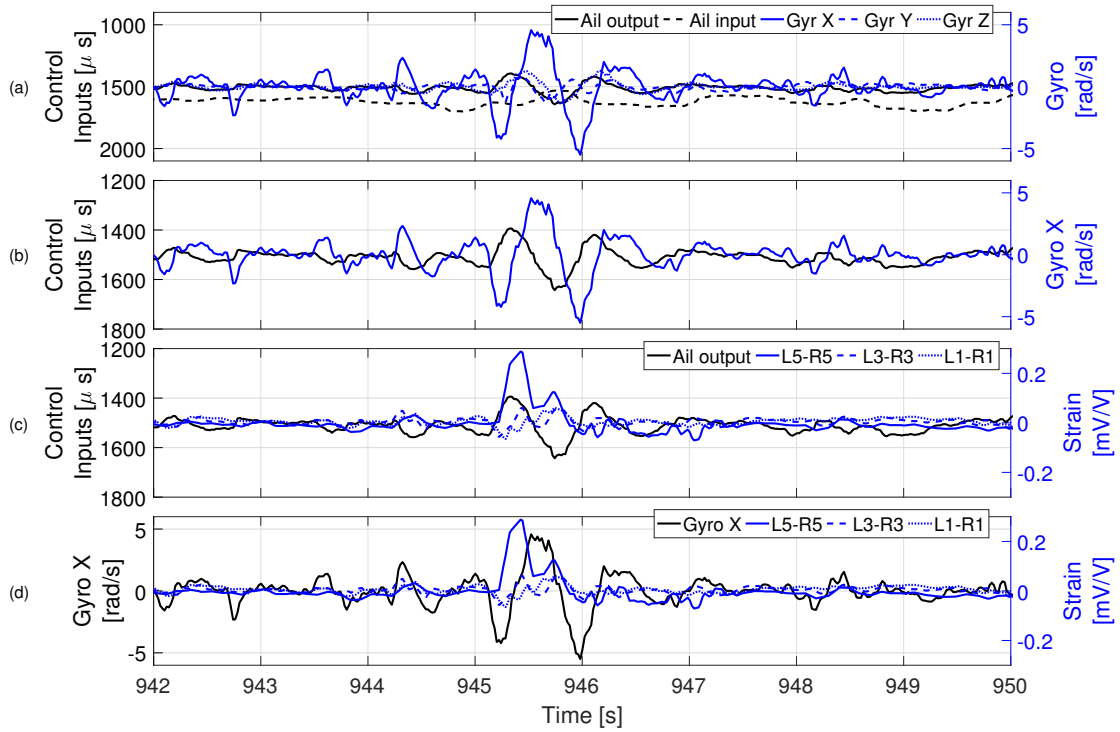
Figure 7. Strain sensing outdoor flight results: response to natural gust.

delimited by $-5° \leq \alpha \leq 6°$, it can be observed that the pressure signal for all sensors changes linearly w.r.t the angle of attack. Flow separation is confirmed by the pressure drop in the signals from sensors $PS01$ and $PS01$ for $\alpha = 14°$. The superimposed XFOIL data allow to infer pressure values for $\alpha = [1°,\ 2°]$, which were not tested. It can be observed that sensor $PS02$ exhibits the biggest change in magnitude w.r.t the angle of attack. The results show that pressure sensing can be used to track the changes in the angle of attack at constant speed. Interestingly it appears that both the pressure sensor and XFOIL results indicated non-linear behaviour on the upper surface, with small pressure drops at $6°$ for $PS01$ and at $8°$ for $PS02$.

An experiment was carried out to identify the characteristics of the pressure signal during stall. In this experiments, the sampling rate of the pressure signal was increased to $200\,\mathrm{Hz}$. Figure 9(a) shows the time histories of the pressure as measured by sensor $PS01$ and the angle of attack of the Bixler 2 aircraft. This test was performed at a wind speed of $16\,\mathrm{m\,s^{-1}}$. In Figure 9(a), the left side scale aids in tracing changes in the pressure signal from sensor $PS01$ (blue solid line) and the right side scale aids in tracing changes in the angle of attack (orange solid line). It can be observed that the pressure changes proportionally w.r.t the angle of attack: first linearly for $0\,\mathrm{s} \leq t \leq 400\,\mathrm{s}$ and then in a non-linear fashion in the range $400\,\mathrm{s} \leq t \leq 700\,\mathrm{s}$. At $t \approx 630\,\mathrm{s}$, the pressure signal variation increases significantly, followed by a marked drop in the magnitude of the signal.

Figure 9(b) shows the time history of the pressure variance computed from the data shown in Figure 9(a), using a 20 samples rolling window. It can be observed that for $0\,\mathrm{s} \leq t \leq 600\,\mathrm{s}$, i.e. angles of attack between $-5°$ and $9°$, the pressure signal variance magnitude does not change significantly. However, when the angle of attack is greater than $10°$ ($t > 600\,\mathrm{s}$), the magnitude of the variance increases sharply.

Figure 9(c) shows a detailed view of the measured pressure and computed pressure variance for the time segment $635\,\mathrm{s} \leq t \leq 640\,\mathrm{s}$. The sudden increase in the magnitude of the variance becomes easier to appreciate in this Figure. The pressure variance magnitude increase was identify as a characteristic sign of stall. In this particular case, a variance value of $500\,\mathrm{Pa}^2$ seems to adequately define a threshold for stall indication. These results suggest that pressure sensing can be used for stall/flow-separation detection.

An outdoor flight experiment was carried using the pressure sensing platform to characterise the pressure signals under "real-life" conditions. For this experiment, data from the pressure, inertial and control outputs, was sampled at $25\,\mathrm{Hz}$, while the control inputs data was sampled at $10\,\mathrm{Hz}$. No augmented stabilisation
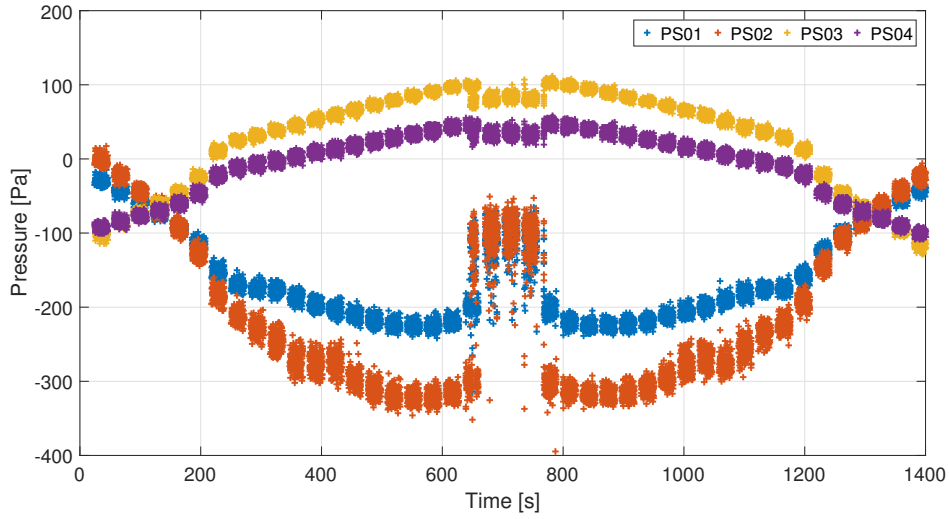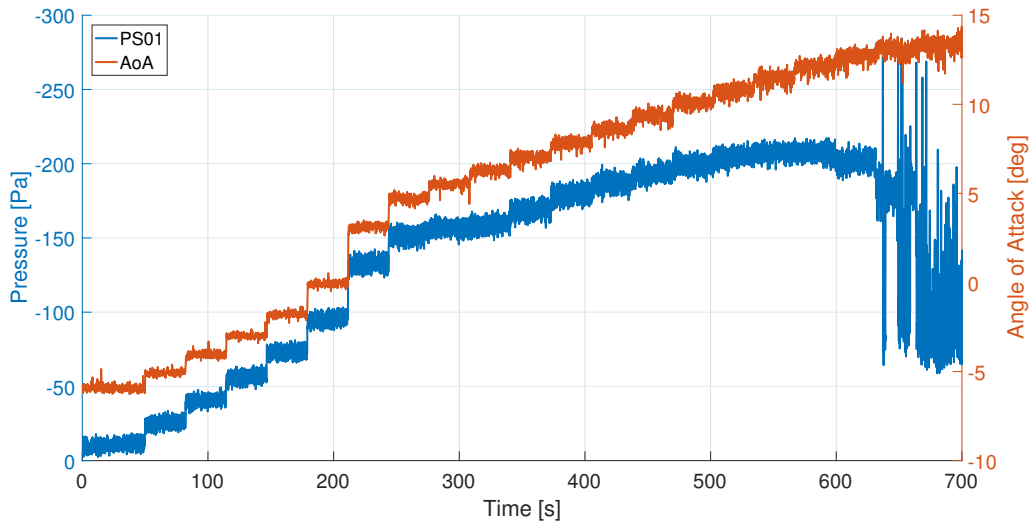
(a) Pressure time histories
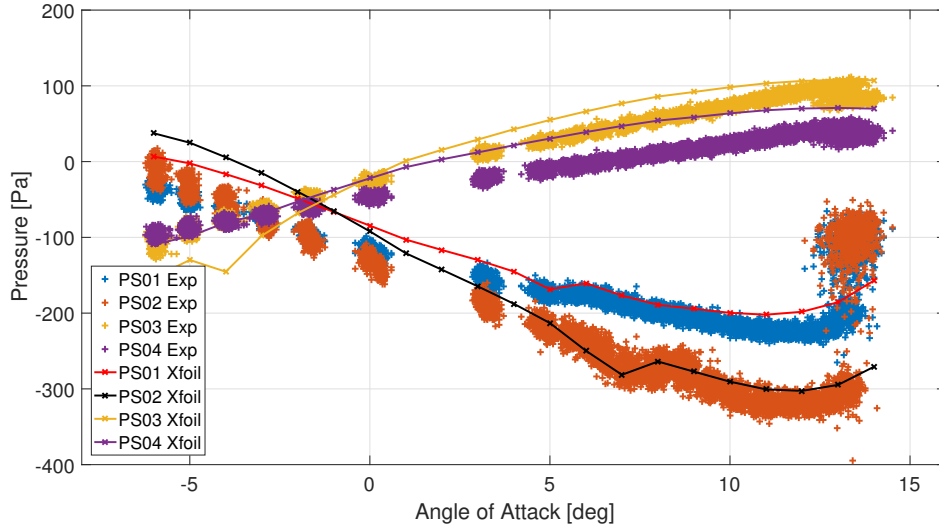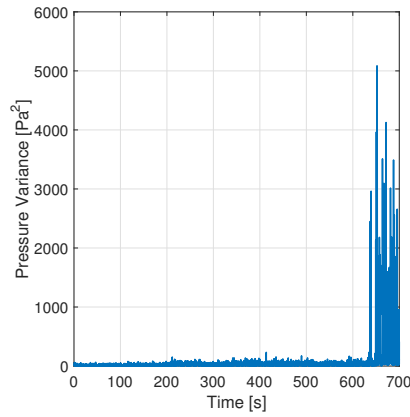

(b) Pressure w.r.t angle of attack

Figure 8. Wind tunnel characterisation results for Bixler at $16 \, \mathrm{m \, s^{-1}}$.

mechanism was in place during this flight, i.e. the autopilot controller was switched off. In this experiment sensor $PS03$ did not work and as a result pressure measurements correspond to the remaining sensors.

Figure 10 shows the time histories response of the pressure sensing platform to an elevator input command in an outdoor flight experiment. Figure 10(a) shows the aileron, elevator, throttle and airspeed time histories. It can be observed that the aileron, elevator and throttle start at a trimmed position and at $t \approx 220.4 \, \mathrm{s}$, the elevator is deflected in order to change the angle of attack, while both the aileron and throttle are held constant. Figure 10(b) shows the body-axes rotational rates time histories, where it can be observed that the motion is dominated by longitudinal dynamics during the manoeuvre, as the pitch rate responds accordingly to elevator input. The aircraft's response to the elevator deflection is describe next. First, the aircraft pitches down (negative pitch rate in Figure 10(c)) and increases its airspeed (Figure 10(a)). Then, the aircraft pitches up increasing its pitch rate and further increasing its airspeed. Finally, the elevator is slowly returned to trim position. Figure 10(c) shows the pressure and angle of attack time histories. Note that the angle of attack reading corresponds to the measured value by the angle of attack sensor described in Section II. It must be noted that the signal from sensor $PS04$ has been inverted. It can be observed that the angle of attack signal is in agreement with the expected aircraft response. Also, the three working sensors

American Institute of Aeronautics and Astronautics

(a) Pressure signal and angle of attack time histories

(b) Pressure variance time history
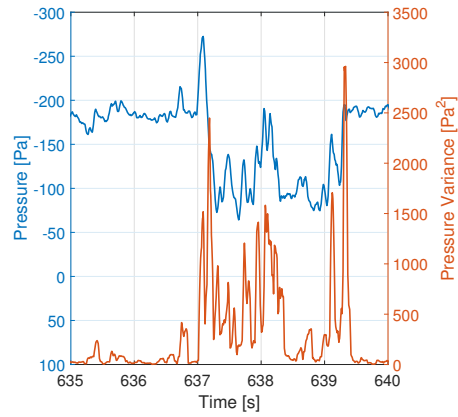
(c) Pressure and pressure variance detailed view

Figure 9. Characterisation of pressure signal during stall.

PS01, PS02 and PS04 tracked the change in angle of attack.

These results show the potential use of pressure sensing for angle of attack tracking under "real-life" conditions. Additionally, the use of distributed sensing increases the robustness against sensor failure when compared to single-point measurements, as shown in this experiment where sensor PS03 did not work but sensors PS01, PS02 and PS04 successfully tracked the change in angle of attack.

Figure 11 shows the time histories response of the pressure sensing platform to a natural gust in an outdoor flight experiment. Figure 11(a) shows the aileron, elevator, throttle and airspeed time histories. It should be noted that the aileron, elevator and throttle start at a trimmed position, with the throttle set to idle. When the commands to the control surfaces are compared to those shown in Figure 10(a), the slow and small amplitude commands indicate that there was no significant inputs from the pilot other than the ones to maintain steady-level flight. Then, at $t \approx 512.9\,\mathrm{s}$, evidence of the aircraft response to a natural gust can be observed in Figure 11(b), where the roll rate magnitude reaches a maximum. This is followed by a pitch rate magnitude peak at $t \approx 513.2\,\mathrm{s}$. The response to the gust is captured by both the pressure and the angle of attack instruments, as shown in Figure 11(c). However, the pressure signal leads the angle of attack measurement and seems to be in phase with roll rate measurement. These results suggest that pressure sensing can be used to detect natural gusts.
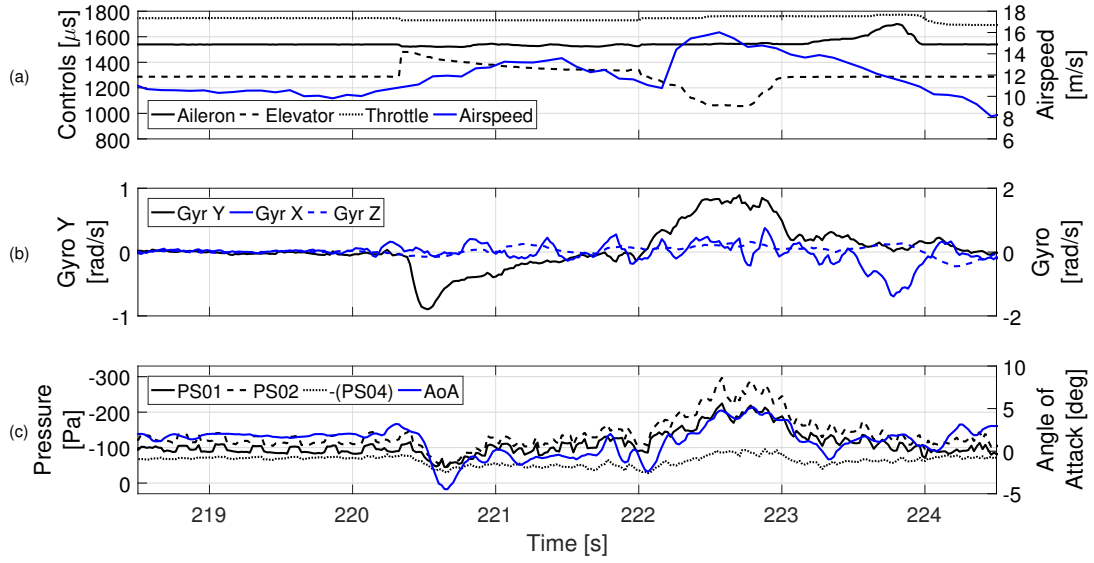
American Institute of Aeronautics and Astronautics

Figure 10. Pressure sensing outdoor flight results: response to elevator input.
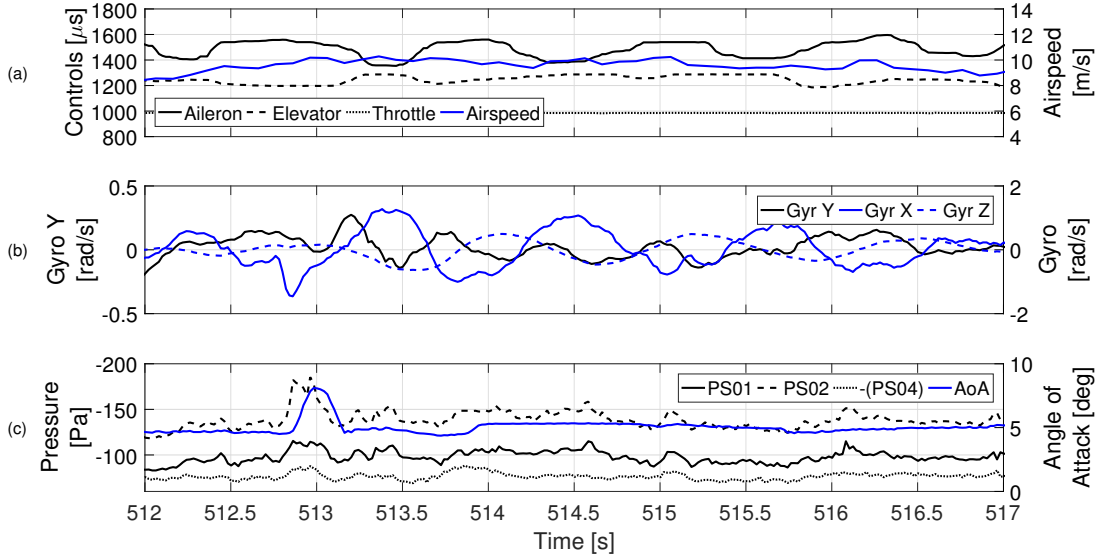

Figure 11. Pressure sensing outdoor flight results: response to natural gust.

IV.   Feedback Control Experimental Results

To illustrate the potential use of distributed sensing to improve the handling qualities of UAVs, experiments with the two instrumented platforms were carried out. Using the strain sensing platform, a series of indoor tests were performed to investigate the feasibility of using the measured strain signals as an input to a feedback roll motion control, with the aim of alleviating the effects of different gust scenarios. Using the strain pressure platform, wind tunnel tests were carried out to explore the feasibility of using pressure sensing for feedback pitch motion control.

American Institute of Aeronautics and Astronautics

A. Strain Based Roll Motion Control

A series of indoors experiments were carried out to characterise the span-wise strain distribution under different testing conditions. The experiments included flights under gust-free conditions, flights under lateral gusts and flights under vertical gusts. The experiments took place in the flying arena at the Bristol Robotics Laboratory. The flying arena is instrumented with a VICON motion tracking system. The system allows tracking the motion and attitude of bodies within the arena. The tracking data provided by the VICON system is made up of the position of the body in a Cartesian coordinate system format (x, y and z coordinates) and the orientation of the body in two formats: Euler angles (roll, pitch and yaw) and quaternion attitude representation. The data acquired by the VICON system is sampled at a frequency of $100\,\mathrm{Hz}$. Each experiment consisted of launching the aircraft through the flying arena using a catapult to improve the repeatability of the experiments. The flight data was recorded using the VICON system and the autopilot on board the aircraft. The aircraft's attitude, rotational rates, accelerations and control outputs were logged at a frequency of $50\,\mathrm{Hz}$ using the Pixhawk, while the strain data was acquired by the strain data acquisition system, then transmitted to the Pixhawk and logged at a frequency of $25\,\mathrm{Hz}$.

With the characteristics of the span-wise strain distribution identified, a strain based proportional controller to reduced the effect of a gust on the aircraft's motion was implemented. The controller uses the difference between the strain signal measured by strain sensor $L5$ and the strain signal measured by strain sensor $R5$ as input signal; sensor $L5$ is located on the left side of the wing and sensor $R5$ is located on the right side of the wing, both at $20\,\mathrm{mm}$ from the centre of the wing. The control is computed using the following expression

$$u = k\left(S_{L5} - S_{R5}\right) \tag{1}$$

with u the control signal, k the controller's proportional gain, S_{L5} the strain signal measured by the centre-left wing strain sensor and S_{R5} the strain signal measured by the centre-right wing strain sensor.

A series of indoors experiments was carried out in order to evaluate a strain feedback controller during a flight with a vertical gust. As with the characterisation experiments, the flight data was recorded using the VICON system and the autopilot on board the aircraft, while the strain data was acquired by the strain data acquisition system, then transmitted to and logged by the Pixhawk. Figure 12 shows the recorded flight data for a vertical gust experiment with strain based feedback control switched on. In this experiment only six of the installed strain sensor signals were acquired and stored.

Figures 12(a) and 12(b) show the indoors flight motion evolution for the test with a vertical gust. In this plot three regions are of interest: take-off ($-3\,\mathrm{m} \leq X \leq 0.4\,\mathrm{m}$), flight through gust ($0.4\,\mathrm{m} \leq X \leq 1.1\,\mathrm{m}$) and post-gust flight ($1.1\,\mathrm{m} \leq X \leq 5\,\mathrm{m}$). Two red dashed vertical lines have been drawn to help identify these regions. The mean gust profile as measured using a sonic anemometer is indicated by the blue vectors. Figure 12(c) shows the aircraft position time histories for the test with a vertical gust. Two red dashed vertical line have been drawn to help identify the time when the aircraft traveled through the gust. This Figure shows the same information as Figures 12(a) and 12(b), albeit as a function of time.

Figure 12(d) shows the aircraft rotational rates time histories for the test with a vertical gust. In the take-off region, it can be observed that the magnitudes of the roll and yaw rates remain small. The magnitude of the pitch rate decreases, reaching a minimum value of approximately $4\,^{\circ}\mathrm{s}^{-1}$ at $t \approx 0.37\,\mathrm{s}$. This is in agreement with the gust-free test. During the flight through the gust region, evidence of the gust effect can be observed in the sharp change in roll rate. After the aircraft leaves the gust region, the aircraft roll dynamics transient response can be observed. The aircraft roll, pitch and yaw rates settle to values close to zero at the end of the flight, i.e. the aircraft reaches level flight.

Figure 12(e) shows the aircraft accelerations time histories for the test with a vertical gust. In the take-off region, only the X and Z accelerations change significantly. During the flight through the gust region, the gust effect is confirmed by sharp change in Z acceleration. After the aircraft transient response to the gust has dampened out, the acceleration signals settle to steady state values.

Figure 12(f) shows the aircraft attitude time histories for the test with a vertical gust. In this figure, it can be observed that the aircraft initial roll angle is about -10°. In the take-off phase region, a significant change in pitch angle can be observed, going from an initial value of approximately 55° to a value close to 0°. The initial roll angle has a non-zero value, but shows a increasing trend towards a value equal to zero until the gust region. During the flight through the gust region, the gust effect is observed in a sharp change in the roll angle. No effect of the gust can be observed in the pitch or yaw angles. After the aircraft leaves
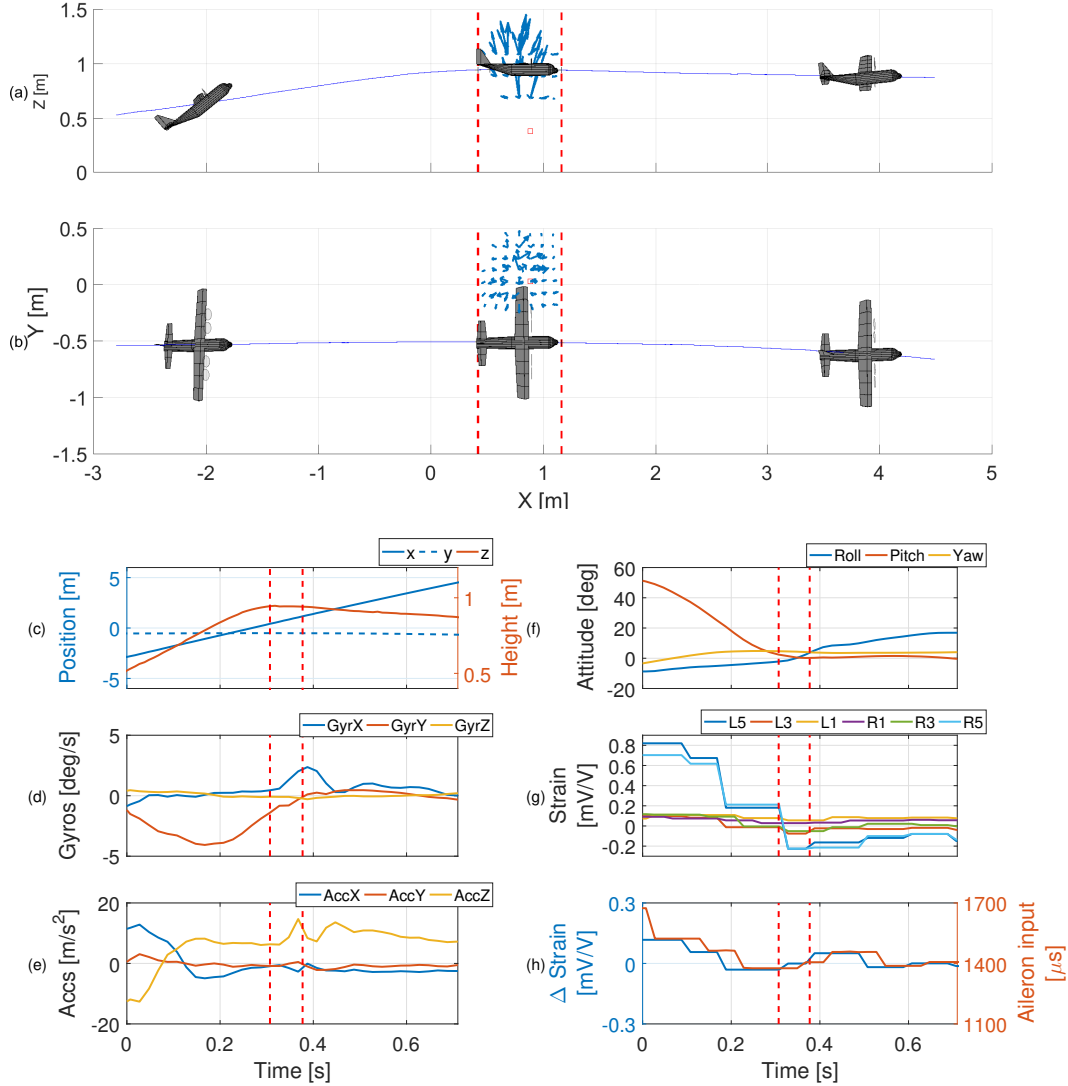
Figure 12. Indoors flight with gust.

the gust region and the aircraft roll transient response has damped out, the roll angle increases slightly until it reaches a value of approximately 20°.

Figure 12(g) shows the measured strain signals time histories for the test with a vertical gust. In the take-off phase region, significant change in the measured strain can be observed, particularly in the signals provided by the sensors close to the centre of the wing. During the flight through the gust region, no clear evidence of the gust effect on the measured strain signal can be observed. It is only after the aircraft has flown through the gust region that a small differential between the left and right centre sensors ($L5$ and $R5$) can be observed: this difference is used as the feedback controller input. It is highly likely that the late identification of the effects of the gust, is related to sampling issues. Given that the time the aircraft spent flying through the gust was around 75 ms and that the strain was sampled once every 40 ms, only one sample is acquired while the aircraft flies through the gust, making it extremely difficult to obtain an early warning in these experimental conditions.

Figure 12(h) shows the time history of the difference between the strain signal measured by the left wing strain sensor $L5$ and the strain signal measured by the right wing strain sensor $R5$ (blue line), as well as the time history of the aileron control command as produced by the autopilot (green line). In the take-off phase

region, a significant difference between the strain signals can be observed, indicating asymmetric wing load. This is likely to be related to the high pitch angle and the non-zero value of both the roll and yaw angles. Once the aircraft enters the gust region, the difference between the strain signals decreases and remains close to zero. After the aircraft leaves the gust region the different loading on each wing is captured by the strain sensors and a maximum strain differential signal of approximately 0.05 is observed. A positive value indicates that the left wing load is smaller that the right wing load. This differential triggers a response from the controller that can be observed in the Aileron input plot. The aileron control command changes proportionally w.r.t. the strain differential signal throughout the length of the test. However, a lag of approximately 40 ms can be observed. It has been identified that this lag is related to processing time in the autopilot system.

To evaluate the feedback control performance the aircraft motion response under different testing conditions is compared. Figure 13 shows the aircraft planar motion and roll angle response under different testing conditions. The different line colors represent different experiment runs for each testing condition: they have been labeled FTx, with x representing the run number.

Figures 13(a) and 13(b) show the aircraft planar motion and roll angle response as a function of the displacement along X for a series of gust-free experiments with no strain feedback. Both Figures show the aircraft flying in a straight level flight with minimal change in the roll angle.

Figures 13(c) and 13(d) show the aircraft planar motion and roll angle response as a function of the displacement along X for a series of lateral gust experiments with no strain feedback. In Figure 13(c) it can be observed that on average the lateral gust had a small effect in the flight direction for this set of experiments with a lateral displacement in the region delimited by $-0.1\,\text{m} \leq y \leq 0.2\,\text{m}$. Figure 13(d) shows that the lateral gust caused a big change on the aircraft's roll angle with an average final roll angle of approximately $40°$.

Figures 13(e) and 13(f) show the aircraft planar motion and roll angle response as a function of the displacement along X for a series of vertical experiments with no strain feedback. In Figure 13(f) it can be observed that on average the vertical gust experiments had a greater effect in the flight direction when compared to the lateral gust experiments with a lateral displacement in the region delimited by $-0.5\,\text{m} \leq y \leq 0.2\,\text{m}$. The average effect of the vertical gust on the aircraft's roll angle is similar to that of the lateral gust, as shown in Figure 13(f) where the average final roll angle was approximately $-40°$.

Figures 13(g) and 13(h) show the aircraft planar motion and roll angle response as a function of the displacement along X for a series of vertical experiments with strain feedback. Figure 13(g) shows that on average the effect of the vertical gust on the flight direction is reduced when compared to the vertical gust experiments without strain feedback control with a lateral displacement in the region delimited by $-0.3\,\text{m} \leq y \leq 0.2\,\text{m}$. The average effect of the vertical gust on the aircraft's roll angle is also reduced when compared to the vertical gust experiments without strain feedback control, as shown in Figure 13(h) where the average final roll angle was approximately $15°$.

Figures 13(i) and 13(j) show the aircraft planar motion and roll angle response as a function of the displacement along X for a series of vertical experiments with inertial feedback. Figure 13(i) shows that the average effect of the vertical gust on the flight direction is similar to the experiments where strain feedback control was used, with a lateral displacement in the region delimited by $-0.4\,\text{m} \leq y \leq 0\,\text{m}$. The average effect of the vertical gust on the aircraft's roll angle is also similar to when strain feedback control was used, as shown in Figure 13(j) where the average final roll angle was approximately $15°$.

These results suggest that, using the current instrumented UAV, strain sensing potentially provides similar performance for gust effects compensation when compared with inertial sensing.

B. Pressure Based Pitch Motion Control

A 1-DOF pitch experiment was carried out in the open-jet wind tunnel with the objective of controlling the pitch angle of the platform via its elevator. Note that in this setup, the pitch angle and the angle of attack are the same. The experiment was carried out at a wind speed of $16\,\text{m\,s}^{-1}$. Two approaches were used to estimate the angle of attack of the platform: the first one used inertial-based measurements from the IMU in the autopilot unit, while the second one used the pressure measurement from sensor $PS02$. The estimated angle of attack was feed into the autopilot preprogrammed pitch controller. For both control approaches, the controller was used with default (out-of-the-box) parameters.

Figure 14 shows the time histories of the inertial-based feedback control test using the pressure sensing Bixler aircraft. The time histories of the measured and reference angles of attack are shown in Figure 14(a).
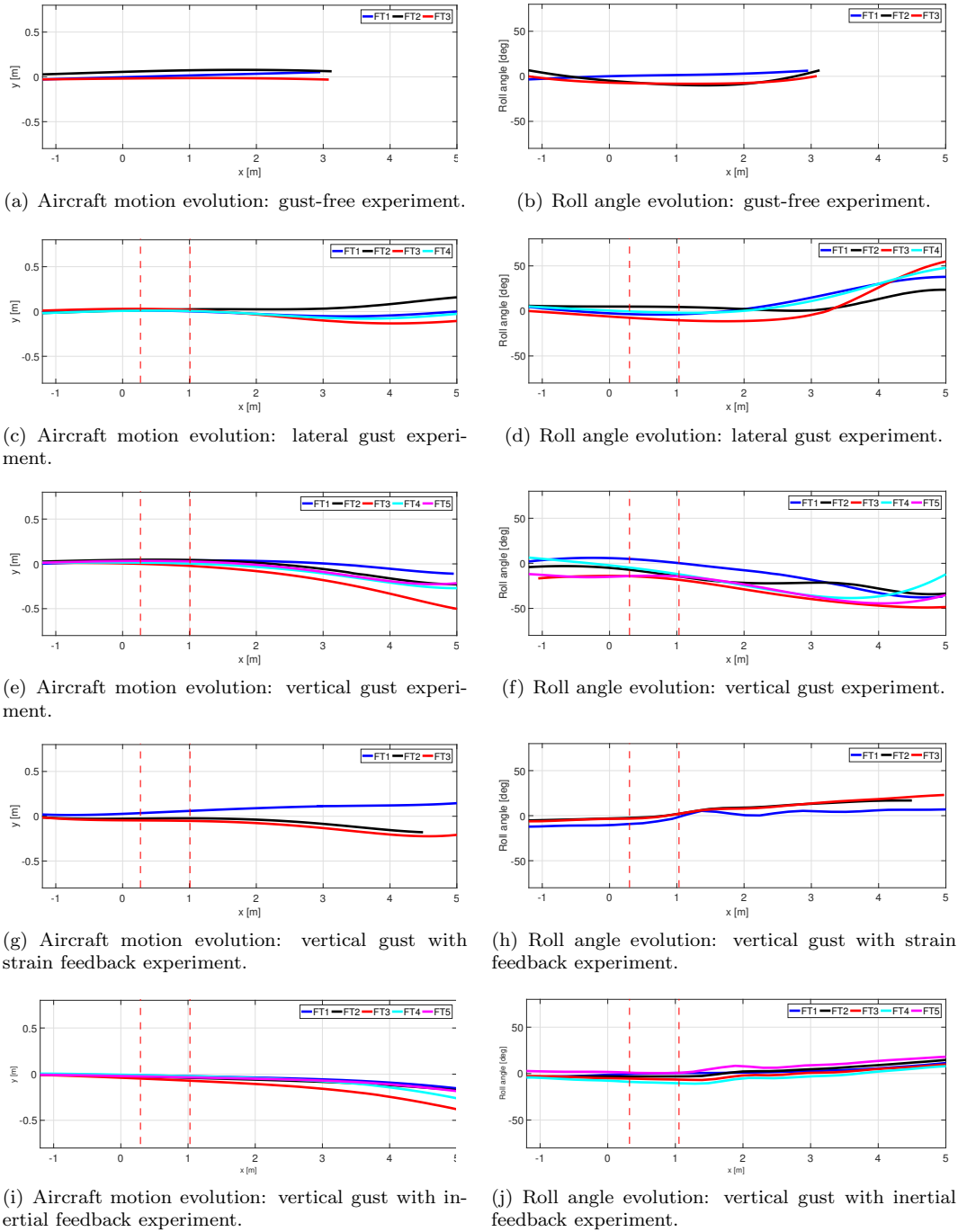
(a) Aircraft motion evolution: gust-free experiment.

(b) Roll angle evolution: gust-free experiment.

(c) Aircraft motion evolution: lateral gust experiment.

(d) Roll angle evolution: lateral gust experiment.

(e) Aircraft motion evolution: vertical gust experiment.

(f) Roll angle evolution: vertical gust experiment.

(g) Aircraft motion evolution: vertical gust with strain feedback experiment.

(h) Roll angle evolution: vertical gust with strain feedback experiment.

(i) Aircraft motion evolution: vertical gust with inertial feedback experiment.

(j) Roll angle evolution: vertical gust with inertial feedback experiment.

Figure 13. Aircraft planar motion and roll angle response under different testing conditions.

A series of manually demanded angle of attack step inputs with different magnitudes were commanded (black dashed line). It can be observed that the measured angle of attack (blue solid line), tracks the reference angle of attack but fails to match the exact demanded value. This angle of attack tracking error is shown in Figure 14(b). As the demanded angle of attack increase so does the angle of attack tracking error.

Figure 15 presents the results of the pressure feedback control test using the pressure sensing Bixler aircraft. Figure 15(a) shows the time histories of the measured and reference angles of attack, as well as the pressure signal from sensor $PS02$. A series of manually demanded angle of attack step inputs with different magnitudes were commanded (black dashed line). In a similar way to the inertial-based experiment, the
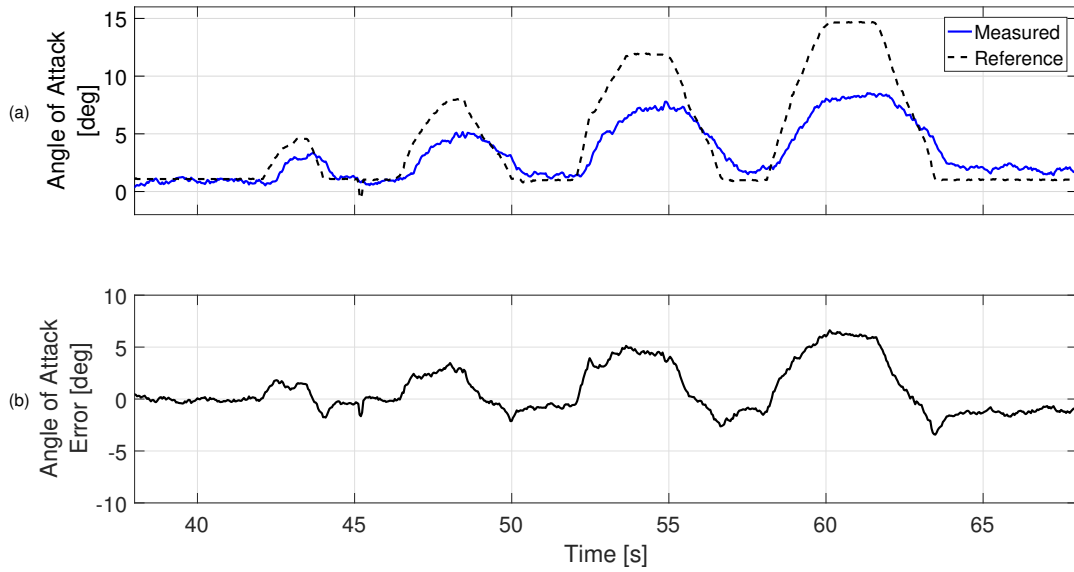
American Institute of Aeronautics and Astronautics

Figure 14. Inertial based pitch feedback control time histories.

measured angle of attack (black solid line), tracks the reference angle of attack but fails to match the exact demanded value. It is interesting to note that even though the magnitude of the demanded angle of attack increases for each input, the measured angle of attack appears to saturate. This can be corroborated by studying the time history of the angle of attack tracking error shown in Figure 15(b). This can be explained by analysing the measured pressure in Figure 15(a), where a value of approximately $-250\,$Pa seems to be the saturation limit. It can be observed that this value coincides with a region of non-linearity in the pressure signal (Figure 8(b)).
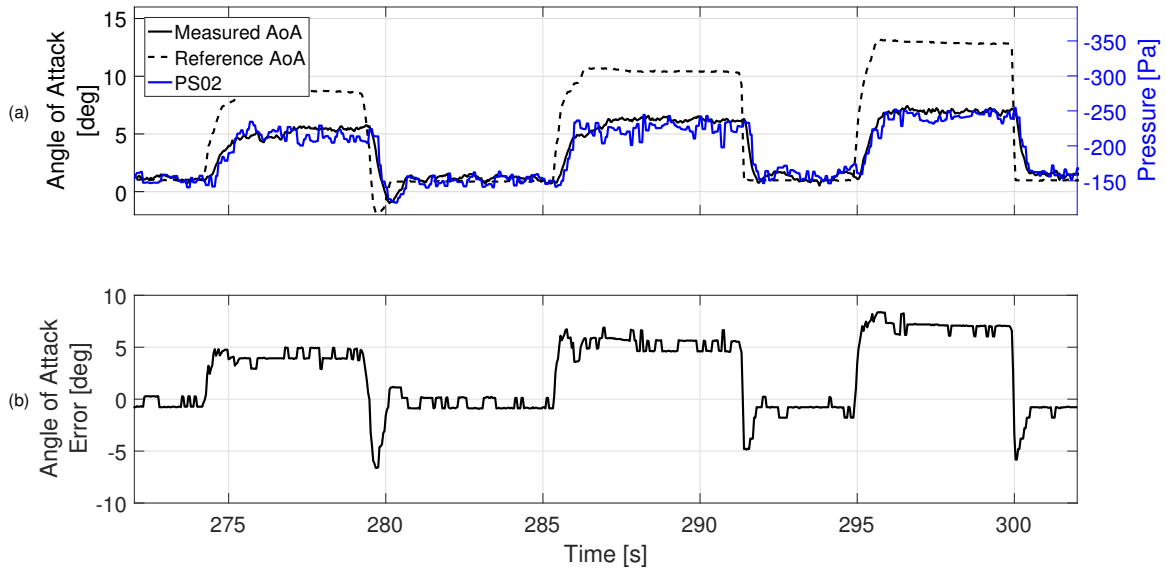

Figure 15. Pressure based pitch feedback control time histories.

These results suggest that, using the pressure sensing platform, pressure sensing potentially provides similar performance for angle of attack control when compared with inertial sensing. Additionally, pressure sensing may pick up on aerodynamic non-linearities.

American Institute of Aeronautics and Astronautics

V. Concluding Remarks

In this paper current research using two UAV platforms instrumented with a distributed array of sensors in order to measure the force (strain) and flow (pressure) distribution acting on their wings was presented. Wind tunnel tests showed a clear linear response between angle of attack and both wing strain and pressure up to stall and then a large increase in signal variation after entering stall. Both sensor types showed clear responses to controlled gusts and there was also evidence of both sensor types responding to natural gusts when flying outdoors. Closed loop control of roll based on strain sensing, and pitch control based on pressure sensing, was achieved and a similar level of performance as IMU based control was demonstrated. In addition, the non-conventional sensors showed the ability to measure properties not encoded by the IMU. The strain sensors encoded total roll moment, proportional to angular roll acceleration in roll and the pressure sensors encoded non-linearities in the aircrafts aerodynamics.

These results show that force sensing and flow sensing both offer rich sources of information for flight control. We have illustrated how these types of signals can be used in some cases in place of conventional inertial based control to achieve similar performance, but this has been through the use of relatively simple control laws. So far the control laws used have not made full use of the rich distributed information available from arrays of sensors. The results show that spanwise sections of the wing undergo different patterns of change in strain and that chordwise features of the airflow can be measured using pressure sensors. This type of distributed information could be integrated as part of a physics based control approach, being based on the estimating the total forces and moments acting on the aircraft.[8–10] Or alternatively this information could be used to achieve a more robust estimate of the aircrafts dynamic state, where the state is estimated based on fusing the signals from a number of different sensors rather than a single sensor. This approach has many similarities to the "mode sensing" approach hypothesized to be used by insects,[5] but raises the question as to what are the appropriate states to measure when fusing information from distributed sensors or from different sensory modalities.

Another interesting aspect illustrated by these results, especially those measurements taken in free-flight, is that control inputs generate response signals in the different sensors. If these sensors signals are to be used for control some expectation of the response of the sensors to the control input appears to be required if the signal is to be used for the detection of external perturbations. This model of the expected response could be based on a conventional flight dynamics modeling approach, augmented with additional sensor models, but this would require extensive characterization of the platform and could be sensitive to changes in the aircrafts properties. An alternative bio-inspired approach would be to learn the correlation between control inputs and the expected sensory response and to filter out the expected sensor response, leaving only the signal generated by any external perturbations. This adaptive filter approach has been suggested as being part of the functional role of the cerebellum in the mammalian nervous system[18] and analogous systems are thought to exist in the nervous systems of other animal groups.

One of the key advantages of distributed sensor arrays is that they enable information to be collected about the local state of the aircraft at different locations. This would appear to be especially useful when an aircraft is highly flexible and cannot reasonably be considered as a single rigid body, such as high-altitude long-endurance (HALE) type aircraft. Another important application area could be in aircraft with distributed control surfaces, or morphing aircraft, where the geometry of local parts of the wing could be controlled in response to local sensor measurements. The characterization of the signals available using distributed force and flow sensor arrays presented here suggests that these application areas could benefit greatly from the development of distributed sensor arrays for flight control.

Acknowledgments

American Institute of Aeronautics and Astronautics

References

[1] Roth, M., "Review of atmospheric turbulence over cities," *Quarterly Journal of the Royal Meteorological Society*, Vol. 126, No. 564, 2007, pp. 941–990, DOI: 10.1002/qj.49712656409.

[2] Mohamed, A., Massey, K., Watkins, S., and Clothier, R., "The attitude control of fixed-wing MAVS in turbulent environments," *Progress in Aerospace Sciences*, Vol. 66, 2013, pp. 37–48, DOI: 10.1016/j.paerosci.2013.12.003.

[3] Brown, R. E. and Fedde, M. R., "Air-flow sensors in the avian wing," *Journal of Experimental Biology*, Vol. 179, 1993, pp. 13–30.

[4] Sterbing-D'Angelo, S., Chadha, M., Chiu, C., Falk, B., Xian, W., Barcelo, J., Zook, J. M., and Moss, C. F., "Bat wing sensors support flight control," *Proceedings of the National Academy of Sciences*, Vol. 108, No. 27, 2011, pp. 11291–11296.

[5] Taylor, G. K. and Krapp, H. G., "Sensory Systems and Flight Stability: What do Insects Measure and Why?" *Insect Mechanics and Control*, edited by J. Casas and S. Simpson, Vol. 34 of *Advances in Insect Physiology*, Academic Press, 2007, pp. 231–316.

[6] Altshuler, D. L., Bahlman, J. W., Dakin, R., Gaede, A. H., Goller, B., Lentink, D., Segre, P. S., and Skandalis, D. A., "The biophysics of bird flight: functional relationships integrate aerodynamics, morphology, kinematics, muscles, and sensors 1," *Canadian Journal of Zoology*, Vol. 93, No. 12, 2015, pp. 961–975.

[7] Mohamed, A., Watkins, S., Clothier, R., Abdulrahim, M., Massey, K., and Sabatini, R., "Fixed-wing MAV attitude stability in atmospheric turbulencePart 2: Investigating biologically-inspired sensors," *Progress in Aerospace Sciences*, Vol. 71, 2014, pp. 1–13, DOI: 10.1016/j.paerosci.2014.06.002.

[8] Shen, H., Xu, Y., and Dickinson, B. T., "Micro Air Vehicle's Attitude Control Using Real-Time Pressure and Shear Information," *Journal of Aircraft*, Vol. 51, No. 2, 2014, pp. 661–671, DOI: 10.2514/1.C032375.

[9] Marino, M. J., Watkins, S., Sabatini, R., and Gardi, A., "Sensing Unsteady Pressure on MAV Wings: a New Method for Turbulence Alleviation," *Applied Mechanics and Materials*, Vol. 629, 8 2006, pp. 48–54.

[10] Yeo, D., Atkins, E. M., Bernal, L. P., and Shyy, W., "Experimental Validation of an Aerodynamic Sensing Scheme for Post-Stall Aerodynamic Moment Characterization," *AIAA Atmospheric Flight Mechanics (AFM) Conference*, AIAA, Boston, Massachusetts, August 2013, DOI: 10.2514/6.2013-4979.

[11] Quindlen, J. and Langelaan, J., "Flush Air Data Sensing for Soaring-Capable UAVs," *51st AIAA Aerospace Sciences Meeting including the New Horizons Forum and Aerospace Exposition*, AIAA, Grapevine (Dallas/Ft. Worth Region), Texas, January 2013, DOI: 10.2514/6.2013-1153.

[12] Samy, I., Postlethwaite, I., Gu, D.-W., and Green, J., "Neural-Network-Based Flush Air Data Sensing System Demonstrated on a Mini Air Vehicle," *Journal of Aircraft*, Vol. 47, No. 1, 2010, pp. 18–31.

[13] Keshavan, J. and Humbert, J. S., "MAV stability augmentation using weighted outputs from distributed hair sensor arrays," *Proceedings of the 2010 American Control Conference*, June 2010, pp. 4445–4450, DOI: 10.1109/ACC.2010.5531002.

[14] Dickinson, B., Baur, J., and Reich, G., "Embedded Sensors for Autonomous Air Systems," *AFOSR Annual Meeting, PM:Les Lee, Mechanics of Multifunctional Materials & Microsystems*, Arlington, Virginia, August 2012.

[15] Thompson, R. A., Evers, J., and Stewart, K., "Attitude control augmentation using wing load sensing-A biologically motivated strategy," *Atmospheric Flight Mechanics Conference*, AIAA, Toronto, Canada, August 2010, DOI: 10.2514/6.2010-7936.

[16] Castano, L., Airoldi, S., McKenna, T., and Humbert, J. S., "Gust rejection using force adaptive feedback for roll," *14th AIAA Aviation Technology, Integration, and Operations Conference*, AIAA, Atlanta, Georgia, June 2014, DOI: 10.2514/6.2014-2588.

[17] Drela, M. and Youngren, H., "XFOIL, Subsonic Airfoil Development System," http://web.mit.edu/drela/Public/web/xfoil/, Online. Accessed: 2016-11-20.

[18] Dean, P., Porrill, J., Ekerot, C.-F., and Jorntell, H., "The cerebellar microcircuit as an adaptive filter: experimental and computational evidence," *Nature Reviews Neuroscience*, Vol. 11, No. 1, 2010, pp. 30–43.